

# Radiation Patterns of RF Wireless Devices Implanted in Small Animals: Unexpected Deformations Due to Body Resonance

Mingxiang Gao, James D. Rosenthal, *Member, IEEE*, Kangling Wu, Germán A. Ramírez, Zvonimir Šipuš, *Senior Member, IEEE*, Stéphanie Lacour, *Member, IEEE*, and Anja K. Skrivervik

**Abstract**—One challenge in designing RF wireless bioelectronic devices is the impact of the interaction between electromagnetic waves and host body tissues on far-field wireless performance. In this paper, we investigate a peculiar phenomenon of implantable RF wireless devices within a small-scale host body related to the deformation of the directivity pattern. Radiation measurements of subcutaneously implanted antennas within rodent cadavers show that the direction of maximum radiation is not always identical with the direction to the closest body–air interface, as one would expect in larger-scale host bodies. For an implanted antenna in the back of a mouse, we observed the maximum directivity in the ventral direction with 4.6 dB greater gain compared to the nearest body–air interface direction. Analytic analysis within small-scale spherical body phantoms identify two main factors for these results: the limited absorption losses due to the small body size relative to the operating wavelength and the high permittivity of the biological tissues of the host body. Due to these effects, the entire body acts as a dielectric resonator antenna, leading to deformations of the directivity pattern. These results are confirmed with the practical example of a wirelessly powered 2.4-GHz optogenetic implant, demonstrating the significance of the judicious placement of external antennas to take advantage of the deformation of the implanted antenna pattern. These findings emphasize the importance of carefully designing implantable RF wireless devices based on their relative electrical dimensions and placement within small-scale animal models.

**Index Terms**—Implanted antennas, directivity pattern, small animals, spherical wave expansion, electromagnetic resonance.

## I. INTRODUCTION

MINIATURE implantable bioelectronic devices are enabling breakthroughs in biomedical research and medical therapy [1]–[4]. In particular, the domain of neuroengineering has grown significantly owing to research in

implantable bioelectronic devices applied to freely behaving animal models [5]–[15]. In order to comply with the size, weight, and power constraints of biomedical applications, the development of wireless, battery-free, and fully implantable devices for neuroscience research requires complex integration [15].

Radio frequency (RF) based wireless devices are a particularly useful technology for bioelectronic devices given their capacity for both wireless power transfer and/or communication [16]–[19], as illustrated in Fig. 1. In the cutting-edge development of neural implants, a properly designed RF wireless power transfer system can realize self-tracking energy transfer [5], [6] and functions such as optogenetic modulation [7]–[9]. RF technology is widely used for wireless data communication, and implanted devices are no exception. To achieve closed-loop neural recording and modulation, RF modules such as Bluetooth Low Energy (BLE) modules are often incorporated into the implant circuits [10]–[12].

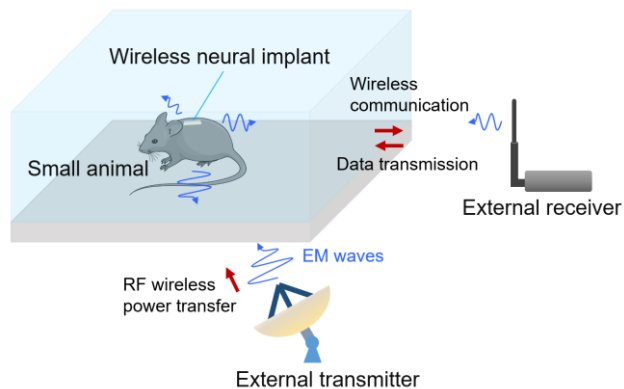


Fig. 1. RF wireless technology is commonly used in neural engineering for wireless power transfer and wireless communication through EM waves.

While high-performance, off-the-shelf wireless communication modules are prevalent, the design of implantable antennas remains challenging. Confined within a miniaturized implant, the body-implanted antenna needs to achieve sufficient link efficiency for successful powering and/or communication. Solutions must consider two important constraints: the material fabrication of the antenna and the EM radiation mechanism of the antennas. In terms of materials, the antenna should be integrated with soft or flexible materials to withstand the mechanical deformations within the body while reducing the impact on neighboring tissues [20]–[23]. From the perspective of EM radiation, the antenna should perform even

© 2023 IEEE. Personal use of this material is permitted. Permission from IEEE must be obtained for all other uses, in any current or future media, including reprinting/republishing this material for advertising or promotional purposes, creating new collective works, for resale or redistribution to servers or lists, or reuse of any copyrighted component of this work in other works. This work was supported in part by the European Union's Horizon 2020 research and innovation program under the Marie-Sklodowska Curie Fellowship grant agreement no. 101027005. (Corresponding author: Prof. Anja K. Skrivervik.)

M. Gao, G. A. Ramirez, and A. K. Skrivervik are with the Microwaves and Antennas Group, Ecole Polytechnique Fédérale de Lausanne, Lausanne, Switzerland.

J. D. Rosenthal, K. Wu, and S. Lacour are with the Laboratory for Soft Bioelectronic Interfaces, Neuro-X Institute, Ecole Polytechnique Fédérale de Lausanne, Geneva, Switzerland.

Z. Šipuš is with Faculty of Electrical Engineering and Computing, University of Zagreb, Zagreb, Croatia.

in the presence of lossy, high permittivity, and heterogeneous biological tissues. This challenge is compounded by significant physiological variations between individual subjects, particularly in behavioral neuroscience research, where small animal models, such as mice and rats, are used in early-stage experimental studies [5]–[14]. Such small-scale host bodies present new challenges for the design and characteristic analysis of implanted antennas due to the high permittivity and high losses of biological tissues, as well as the body geometry that is small relative to the operating RF wavelength.

To analyze the radiation mechanisms of implanted antennas, a commonly used research approach is to simplify the models of the implanted antenna while maintaining the key parameters such as the permittivity of biological tissues and macroscopic dimensions of both the implanted source and the host body [24]–[26]. A series of studies have been conducted with the help of simplified models, known as canonical body models, to analyze the fundamental limits and optimal radiation of body-implanted antennas [27]–[37]. The two most popular canonical body models are the multi-layer planar model and the multi-layer spherical model. Compared to the planar model with an infinite half-space lossy medium, the spherical model has tremendous advantages in refining the phantom geometry with limited dimensions and different curvatures of the body–air interface.

Most existing studies on the modeling of implanted antennas choose to have large geometric dimensions of the host body, e.g., the spherical body dimensions of around 10 cm or more, to model human heads or other large body parts. On this basis, due to the high loss properties of biological tissue, the maximum power density or the maximum gain of the antenna can be found in the direction of the shortest path from the implant to the body–air interface [38]. However, for small animal bodies, the radiation characteristics of implanted antennas become more complex. As the body dimensions decrease, the losses caused by biological tissues become less significant, leading to higher radiation efficiency. Furthermore, due to the high permittivity of most biological tissues, strong reflections of EM waves at the body–air interfaces can affect the EM field distribution inside the body, thereby changing the far-field radiation pattern.

In this paper, we investigate the peculiar radiation characteristics of implantable RF wireless devices within small animals, i.e., deformations of directivity due to the small-scale host bodies. The approach of this paper is to introduce the phenomena through experiments and interpret the mechanisms behind using simplified models, concluding with discussions and related applications. The phenomena were first observed in far-field measurements of antennas implanted in rodents. To explore these results, we have developed an experimental setup to test the implanted antennas and measure their radiation patterns when implanted subcutaneously in mouse and rat cadavers. The deformation of radiation patterns makes the direction of maximum gain difficult to predict, with it sometimes appearing in the direction of a relatively long path from the implant through the body.

To analyze the mechanisms associated with the small animal

body effects on the directivity pattern, a simplified spherical body model with an offset implanted antenna is introduced. By means of spherical wave expansion and full-wave simulations, we provide an in-depth analysis of the contribution of higher-order spherical modes and EM resonance effects in small-scale bodies. Moreover, a practical case of RF wireless power transfer to an implantable device is given to illustrate the significance of the analyzed characteristic in the design of wireless system.

The paper is structured as follows: in Section II, the radiation pattern measurements for a dipole antenna subcutaneously implanted in the back of a mouse and a rat are presented. In Section III, a simplified model for antennas implanted in small animals is proposed, and an analytic procedure utilizing spherical harmonics is introduced. In Section IV, two scenarios of the simplified model with different scales are compared, providing insight into the mechanism of directivity enhancement and the EM resonances of small animal bodies. In Section V, we present test results of an implantable optogenetic probe powered by RF wireless links, showing how the insights from previous sections might be applied. The paper concludes with a summary and suggestions for future work in Section VI.

## II. MEASUREMENTS OF IMPLANTED ANTENNAS WITHIN SMALL ANIMALS

### A. Experimental setup

To investigate the radiation characteristics of implantable RF wireless devices within small animals, we conducted several antenna measurements on a mouse and a rat cadaver. These small animals were obtained in accordance with EPFL's Animal Research Ethics Committee under license VD3290.1.

As shown in Fig. 2(a), the implantable antenna is a planar dipole antenna fabricated on a flexible printed circuit board (PCB), which is based on a polyimide substrate ( $\epsilon_r = 3.5$ ) with a total thickness of 0.1 mm. Since the PCB has only a single layer of copper and the dipole antenna is balanced fed, the reference impedance is chosen to be 100  $\Omega$ . The antenna feed uses a differential matching network [see Fig. 2(b) for detailed parameters] for impedance matching to a 100- $\Omega$  coplanar stripline on the same PCB.

The input impedance of an implanted antenna depends on various factors, including its own geometry, the implantation depth, the tissue composition, and the geometry of the host body. To tune the antenna to resonate in the 2.4-GHz industrial, scientific, and medical (ISM) band (2.4 to 2.5 GHz), we first measure the input impedance of the implanted antenna without a matching network using a vector network analyzer (8720D, HP). The specific parameters of the matching network are then calculated using circuit theory based on the measured input impedance. To match the unbalanced 50- $\Omega$  port of the measurement equipment, a 50  $\Omega$  (unbalanced) to 100  $\Omega$  (balanced) ceramic chip balun (2450BL15K100E, Johanson Technology) is introduced between the 50- $\Omega$  coaxial cable and the 100- $\Omega$  balanced coplanar stripline, as illustrated in Fig. 2(a). For biocompatibility and corrosion protection, the implanted part of the antenna is encapsulated with flat films made of

Ecoflex on top and bottom for a total thickness of 1 mm.

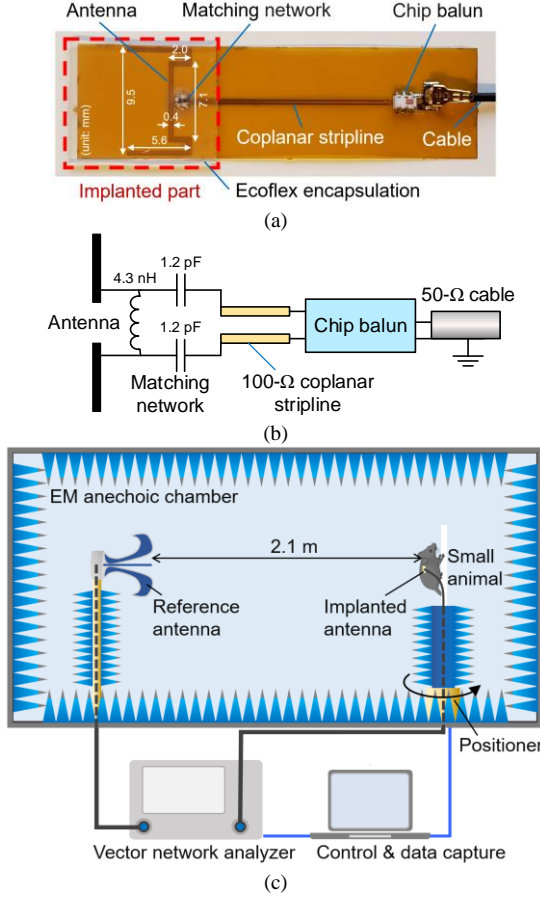


Fig. 2. (a) Photograph of the implantable dipole antenna. (b) Schematic circuit diagram of the implantable dipole antenna. (c) Schematic of the experimental setup for far-field measurements of the implanted antenna within a mouse cadaver.

An experimental setup for far-field measurements of implanted antennas was built in an EM anechoic chamber, as illustrated in Fig. 2(c). A quad-ridge horn antenna (QH400, MVG Industries) is used as a reliable reference antenna in the anechoic chamber, which is fixed at 2.1 m from the antenna under test for far-field measurement. The polarization direction of the reference antenna is always set to coincide with the orientation of the implanted dipole antenna.

### B. Characterization of an Antenna Implanted in a Mouse Cadaver

We first investigate the radiation characteristics with respect to a subcutaneous antenna dorsally implanted in a female adult mouse cadaver euthanized 1 hour prior to the measurements. As shown in Fig. 3, the antenna is implanted subcutaneously in the coronal plane and above the vertebrae, with the dipole oriented parallel to the spinal column. The mouse body with the antenna is mounted on an acrylic frame that can be rotated to measure the far-field radiation pattern in the azimuth plane.

The measured reflection coefficient magnitude of the implanted antenna with the proper matching network design is given in Fig. 4(a). This antenna operates in the 2.4-GHz ISM band, with a  $-10$ -dB bandwidth of 278.7 MHz (11.4%). Moreover, Fig. 4(b) shows the input impedance spectrum of the

implanted antenna after adding the matching network. The antenna resonates well at 2.45 GHz and the real part of the impedance is nearly  $100\ \Omega$ , i.e., the characteristic impedance of the feeding coplanar stripline.

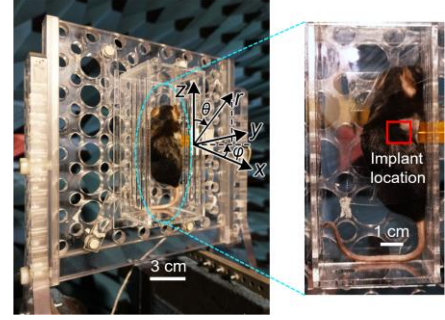


Fig. 3. Photograph of the antenna subcutaneously implanted in the dorsal of a mouse cadaver.

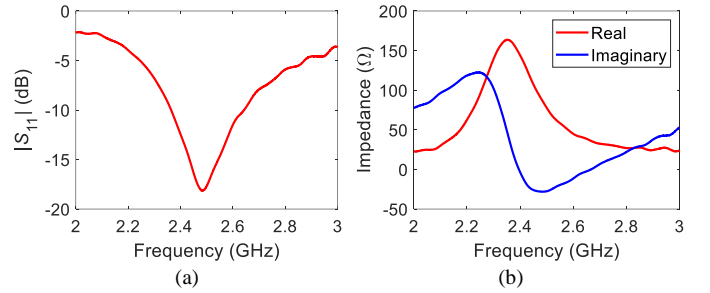


Fig. 4. Measured (a) reflection coefficients  $|S_{11}|$  and (b) input impedance of the antenna implanted subcutaneously in a mouse cadaver.

The measured radiation patterns (normalized to the maximum value) in the  $x$ - $y$  (azimuth) plane and the  $x$ - $z$  (elevation) plane at 2.45 GHz are illustrated in Fig. 5(a) and Fig. 5(b), respectively. Consistent with the coordinate system shown in Fig. 3, the direction of  $\varphi = 0^\circ$  in the  $x$ - $y$  plane or  $\theta = 90^\circ$  in the  $x$ - $z$  plane represents the positive direction of the  $x$ -axis, i.e., the shortest forward wireless link from the implant location to the mouse dorsal interface and reaching the free space. Likewise, the direction of  $\varphi = 180^\circ$  in the  $x$ - $y$  plane or  $\theta = 270^\circ$  in the  $x$ - $z$  plane represents the negative direction of the  $x$ -axis, that is, the backward wireless link through the entire mouse body to the ventral body-air interface. Overall, as illustrated in Fig. 5, the radiation patterns of the implanted antenna are significantly deformed compared to the results of the unimplanted antenna case, which behaves as a typical dipole antenna.

In fact, we notice that the small animal body does not directly attenuate the radiation pattern according to the implantation depth or tissue characteristics of the different radiation directions. For the radiation pattern in the  $x$ - $y$  plane [Fig. 5(a)], the maximum directivity does not occur in the positive direction of the  $x$ -axis, but in almost the exact opposite direction, i.e.,  $\varphi = 170^\circ$ . The difference in gain between these two directions reaches 4.6 dB, a considerable amount for wireless link efficiency.

From the perspective of the pattern lobes, the maximum directivity corresponds to a narrow beamwidth, which indicates the contribution of higher-order modes excited by the host

body. The measured maximum gain in the  $x$ - $y$  plane is  $-12.72$  dBi. In other directions, the radiation pattern consists of several wide lobes, and the peak value on the two sides of the mouse (i.e.,  $60^\circ < \varphi < 120^\circ$  and  $240^\circ < \varphi < 300^\circ$ ) is only around 2 dB less than the maximum directivity. A similar gain-enhanced phenomenon can be observed in the radiation pattern in the  $x$ - $z$  plane (Fig. 5) as well.

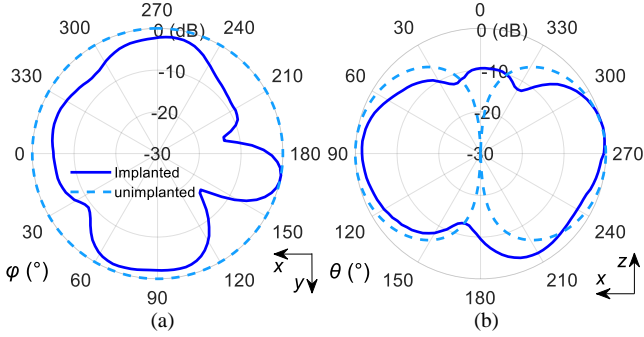


Fig. 5. Measured radiation patterns (solid lines) in (a)  $x$ - $y$  plane and (b)  $x$ - $z$  plane at 2.45 GHz, where the antenna under test is implanted subcutaneously in a mouse cadaver. For comparison, the radiation patterns (dashed lines) of the unimplanted antenna placed in free space are also presented via CST Microwave Studio Suite simulation.

The above analysis clarifies that, in the azimuth plane, placing an external antenna on one of the sides of the mouse body can achieve an efficient and robust wireless link; in the elevation plane, the appropriate external antenna location is just below or above the mouse body. For situations where the mouse body can be immobilized, the highest wireless link efficiency can be utilized by choosing the backward wireless link, which is particularly desirable for wireless power transfer due to the tight link budget.

### C. Characterization of an Antenna Implanted in a Rat Cadaver

Applying the same measurement procedure, we further investigate the radiation performance of an antenna subcutaneously implanted in the back of a rat. Given the larger size of rats, three different subcutaneous implant locations (denoted as L1, L2, and L3 along the spine from the back of head to the base of the tail) in the coronal plane and above the vertebrae of the rat body were taken for measurement, with the dipole oriented perpendicular to the spinal column in all cases (Fig. 6). The implanted dipole antenna was tuned to resonate in the 2.4-GHz ISM band. As a result, the measured radiation patterns at 2.45 GHz for implant locations L1, L2, and L3 are shown in Fig. 7, respectively.

The radiation patterns of the implanted antennas at different implant locations have significant variations, which are attributed to the alteration in the amplitude and phase of excited higher-order modes. At implant location L1 at the back of the rat head, the radiation patterns [see Fig. 7(a)] exhibit a similar gain-enhanced phenomenon to that observed in the mouse cadaver. However, for implant locations L2 and L3 above the rat spine, the direction of maximum radiation is now identical to the direction of the shortest path outside of the body, as it would be for a large host body. This is explained by the larger

volume of biological tissues surrounding the antenna in this case the antenna (i.e., occupy the near-field region) compared to L1, which is closer to the rat head. As shown in Fig. 7(b) and (c), the maximum directivities occurred in the positive direction of the  $x$ -axis, which represents the shortest path to the body-air interface in the forward wireless link. This can be attributed to the fact that the wireless path through the entire rat body is no longer advantageous due to the increased near-field losses and propagation losses. The measured maximum gains in the  $x$ - $y$  plane are  $-19.38$  dBi,  $-18.18$  dBi, and  $-20.02$  dBi for the three implant locations L1, L2, and L3, respectively.

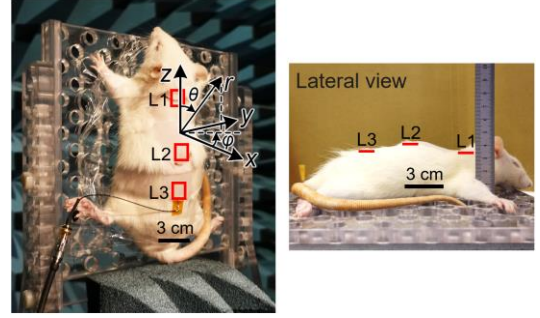


Fig. 6. Photograph of the antenna implanted in the dorsal of a rat cadaver, with three different implant locations annotated as L1, L2, and L3.

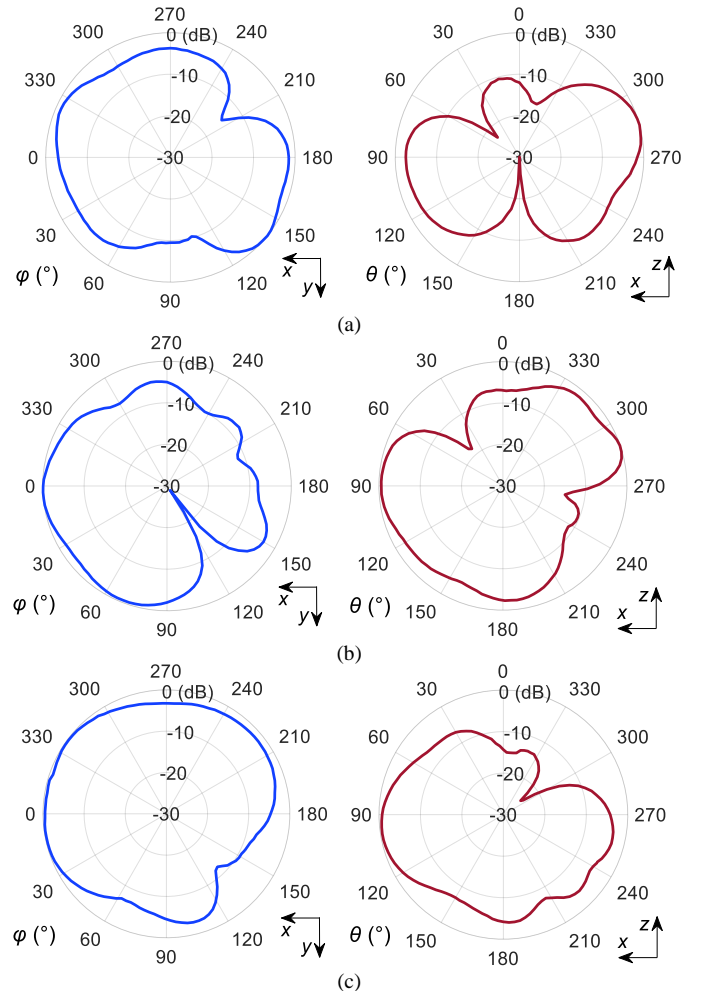




Fig. 7. Measured radiation patterns in the  $x$ - $y$  plane (left) and  $x$ - $z$  plane (right) at 2.45 GHz, where the antenna is implanted subcutaneously in a rat cadaver at implant locations (a) L1, (b) L2, and (c) L3.

### III. MODELING OF IMPLANTED ANTENNAS WITHIN SMALL ANIMALS

In this section, we propose a reasonably simplified model for representing the radiation characteristics of an antenna implanted into a small animal body. The model consists of an elementary EM source (i.e., an electrically small antenna) placed in a spherical body phantom. This model is known as the spherical body model. Although the model with a simplified homogeneous phantom cannot be directly applied to real-world implants, it nonetheless provides an efficient means for understanding the working mechanism of the implanted antenna within a small-scale host body.

#### A. Simplified model of antennas implanted in small animals

In contrast to EM waves radiated from an antenna in free space, the EM waves from an implanted antenna first propagate into a lossy medium before reaching free space at the body-air interface. Therefore, a lossy body phantom surrounding the implanted antenna is introduced in the proposed model. Subject to the miniature size of implants, implanted antennas are in most cases electrically small, making elementary EM sources suitable for modeling.

As a practical case of interest, we consider an electrically small antenna subcutaneously implanted dorsally in a mouse, as shown in Fig. 8(a), which represents a commonly used scenario of an implant in neuroengineering research [15]. Although most biological tissues are highly lossy [39], the limited dimensions of a small animal body allow radiated EM waves to reach free space in any direction with a short in-body path through lossy tissues.

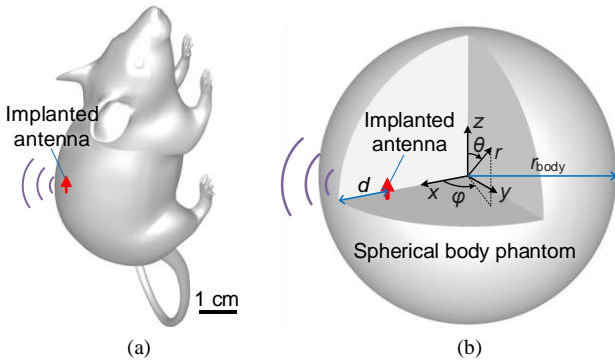


Fig. 8. (a) View of a practical implantation case: An electrically small antenna implanted dorsally in a mouse body. (b) View of a simplified spherical body model where an elementary EM source is implanted eccentrically in a spherical body phantom.

To investigate the radiation mechanism of this type of implanted antenna using an analytical model, we need to simplify the realistic small animal body on a macro scale. We can simplify the organs and biological tissues to homogeneous body tissue in order to focus our analysis on scattering and reflection from the body-air interface. Similarly, the geometric structure of the body can be simplified as a sphere while retaining the basic dimensions. These simplifications provide

accessible models for theoretical analysis at the expense of computational accuracy far behind numerical simulations. For scenarios of shallow implants within small-scale host bodies, spherical body models with small dimensions and similar permittivity of biological tissues become suitable choices.

In the spherical body model, we implant an elementary EM source eccentrically in a spherical body phantom of radius  $r_{\text{body}}$ , as illustrated in Fig. 8(b). The orientation of the source is parallel to the closest outer interface of the body phantom, which is commonly used in practical designs. As the host body becomes small, such as a rodent body, the body phantom no longer causes severe propagation losses of the radiated EM waves. We consider a simplified homogeneous body phantom composed of muscle only, which is known as one of the most highly lossy biological tissues. The four-region Cole-Cole model based on measurement data is used to represent the complex permittivity of biological tissues as a function of frequency [39].

#### B. Analytical Method in Electromagnetics: Spherical Wave Expansion

For the simplified spherical body model, the solution procedure makes use of the spherical wave expansion (SWE) method, allowing us to analytically compute the EM fields in full space [40]–[44]. The complex EM field quantities  $\mathbf{E}$  and  $\mathbf{H}$  in regions without the presence of any source are expressed using vector spherical harmonics  $\mathbf{M}$  and  $\mathbf{N}$ :

$$\begin{Bmatrix} \mathbf{E} \\ -i\eta\mathbf{H} \end{Bmatrix} = \sum_{n,m} a_{mn} \begin{Bmatrix} \mathbf{M}_{mn} \\ \mathbf{N}_{mn} \end{Bmatrix} + b_{mn} \begin{Bmatrix} \mathbf{N}_{mn} \\ \mathbf{M}_{mn} \end{Bmatrix}, \quad (1)$$

where  $\sum = \sum_{n=1}^{+\infty} \sum_{m=-n}^n$ ,  $a_{mn}$  and  $b_{mn}$  are the spherical modal coefficients,  $m$  and  $n$  are the mode indexes,  $\eta$  is the intrinsic impedance in the medium, and  $\mathbf{M}_{mn}$  and  $\mathbf{N}_{mn}$  are both functions of the scalar function  $\psi_{mn}$ . More specifically, here

$$\psi_{mn} = (1/kr) \hat{Z}_n(kr) P_n^{(m)}(\cos\theta) e^{im\phi}, \quad (2)$$

which is the solution of the scalar Helmholtz equation in spherical coordinates of  $(r, \theta, \phi)$ , where  $\hat{Z}_n$  represents either the spherical Bessel functions  $\hat{B}_n$  or the Hankel functions  $\hat{H}_n$  in Schelkunoff type [41],  $k$  denotes the wavenumber of the considered medium, and  $P_n^{(m)}$  denotes the associated Legendre functions. Detailed derivations can be found in [45].

By analytically calculating the radiated power density and the total radiated power, we can directly plot the overall directivity pattern of the implanted antenna and the directivity patterns for specific spherical modes according to the antenna theory. In this analysis, the lossless encapsulation surrounding the source can be omitted as it is always electrically small and has limited effects on the directivity pattern according to the equivalence principle [41].

### IV. ELECTROMAGNETIC RESONANCE EFFECTS IN SMALL BODIES

In this section, the EM resonance effect of a small-scale host body is theoretically investigated by comparing the radiation

patterns of implanted antennas using the spherical body model. The SWE method described in Section III enables us to analyze the overall directivity pattern and the directivity patterns by looking into different spherical modes. These results can be used to determine the dominant modes of antenna radiation and the mechanism by which the overall radiation pattern is formed. In addition, full-wave simulations using the time domain solver of CST Microwave Studio Suite further demonstrate properties of the EM field distribution within the small body.

Two scenarios are investigated to compare the radiation pattern of an implanted antenna. As described in Table I, Scenario 1 represents a small-scale body model, which is close to the dimension of a mouse body, and Scenario 2 represents a large-scale body model, which is close to the dimension of a monkey's head. In both scenarios, an offset implanted antenna is used as the excitation source.

TABLE I  
DIMENSIONS OF TWO SCENARIOS FOR SPHERICAL BODY MODEL

Scenario	Phantom category	$r_{\text{body}}$	$d$
Scenario 1	Small scale	2 cm	1 cm
Scenario 2	Large scale	6 cm	1 cm

#### A. Analysis of a small-scale spherical body model

To model the body of a small animal like a mouse, Scenario 1 has a spherical phantom radius  $r_{\text{body}}$  of only 2 cm, as shown in Fig. 9(a). The phantom is composed of muscle with a complex permittivity of  $\hat{\epsilon}_r(\omega) = \epsilon'_r(\omega) - i\epsilon''_r(\omega) \approx 52.79 - i12.77$  at 2.40 GHz, which is also the operating frequency of the implanted source. To ensure that the number of excitation modes used in the SWE method is sufficient to provide accurate results, the number of spherical modes is truncated using the method demonstrated in [46, Section II. C.]. This method estimates the highest order of spherical mode as a function of the model geometry.

In the full-wave simulation, the Hertzian dipole used in the SWE model is replaced by a realistic dipole antenna as the new excitation, as shown in Fig. 9(a). This is an electrically short dipole antenna consisting of two conductive cylinders with a radius of  $r_{\text{dip}} = 0.1$  mm, a feeding gap width of 0.1 mm, and an overall length of  $L_{\text{dip}} = 2$  mm. The antenna is surrounded by a lossless air sphere to roughly represent the encapsulation of the implantable device. The radius of the encapsulation is  $r_{\text{impl}} = 1.2$  mm, which is electrically small as most advanced implants.

The overall directivity pattern of Scenario 1 can be appreciated in Fig. 9(b). The obtained radiation patterns exhibit a distinctive feature: The maximum directivity does not appear in the positive  $x$ -direction (i.e., from the implanted source to the closest body–air interface, which is the commonly expected direction of the maximum), but in the opposite direction. This peculiar phenomenon suggests that small-scale host bodies have complex effects on the radiation characteristics of the implanted antenna. Specifically, the main lobe has a maximum directivity of 5.09 dBi, while the directivity in the positive  $x$ -direction is 1.61 dBi. The Simulated results are also displayed in the 2-D pattern in Fig. 9(b), which are in good agreement

with the results obtained with the SWE method.

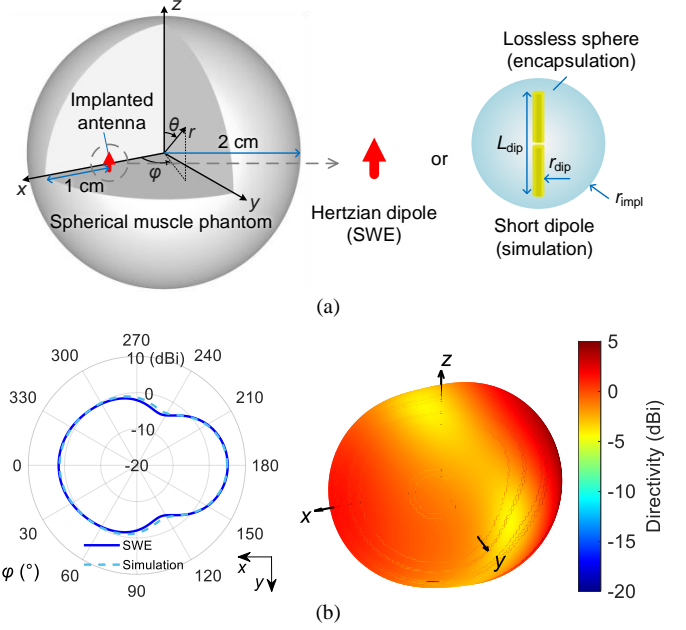


Fig. 9. (a) View of Scenario 1, a small-scale spherical body model. (b) Overall directivity patterns of Scenario 1 computed with the SWE method. The 2-D pattern shows the directivity pattern on the  $x$ - $y$  plane with the variable of  $\phi$ , where the simulated pattern is also displayed. Similar demonstrations are used in the following figures.

By decomposing the radiated EM waves into different spherical modes, insight can be gained into the impact of small-scale host bodies on the directivity deformation. We have grouped spherical modes having the same index  $n$  into corresponding sets (i.e., each set contains  $2n + 1$  modes with index  $m$  between  $-n$  and  $n$ ). Fig. 10 shows the directivity patterns of Scenario 1 for specific sets of spherical modes with the order of  $n = 1, 2$ , and  $3$ , respectively. Since for each index  $n$  we are actually considering a linear combination of  $2n + 1$  modes different amplitude and phase distributions can be achieved. For quantitative evaluation, we calculate the normalized radiated power (with respect to the total radiated power) and the phase difference in the positive and negative  $x$ -directions (i.e., the shortest and longest paths from the implant to the body–air interface) for different sets of spherical modes, as listed in Table II.

TABLE II  
RADIATED POWER AND PHASE DIFFERENCES OF SPHERICAL MODES IN SCENARIO 1

Mode index $n$	1	2	3	4	5
Normalized radiated power	79.08%	20.52%	0.39%	$5.1 \times 10^{-5}$	$9.7 \times 10^{-8}$
Phase difference in positive $x$ -direction	$0^\circ$	$92.09^\circ$	$-133.80^\circ$	$4.82^\circ$	$153.46^\circ$
Phase difference in negative $x$ -direction	$0^\circ$	$20.55^\circ$	$-7.01^\circ$	$-59.25^\circ$	$-72.16^\circ$

According to the results presented in Table II and Fig. 10, the dominant modes are the fundamental spherical modes with  $n = 1$ , while the spherical modes with  $n = 2$  and  $3$  also contribute essentially to the overall directivity formation due to their

enhanced lobes. The difference in directivity between the positive and negative  $x$ -directions is of interest because it acts as an indicator of the internal mechanism behind the deformation of the directivity pattern and the enhancement of the directivity in a specific direction.

As shown in Fig. 10, due to the limited dimension of the lossy phantom, the pattern shapes for specific spherical modes are almost symmetric with respect to the plane of symmetry  $x = 0$ , especially for the sets of spherical modes with  $n = 1$  and 2. In the positive  $x$ -direction, the directivity contributed by the fundamental modes with  $n = 1$  is decreased as the phase differences to higher-order spherical modes with  $n = 2$  and 3 exceed the range of  $[-90^\circ, 90^\circ]$ , i.e., a cancellation of the amplitude occurs. However, in the negative  $x$ -direction, when the EM waves of the spherical modes with  $n = 1, 2$ , and 3 are superimposed, the final directivity is effectively enhanced due to the small phase difference between them. As a result, on the overall directivity pattern in Fig. 9(b), we can observe a peculiar phenomenon: The directivity in the negative  $x$ -direction is significantly enhanced, even exceeding that in the positive  $x$ -direction by more than 4 dB.

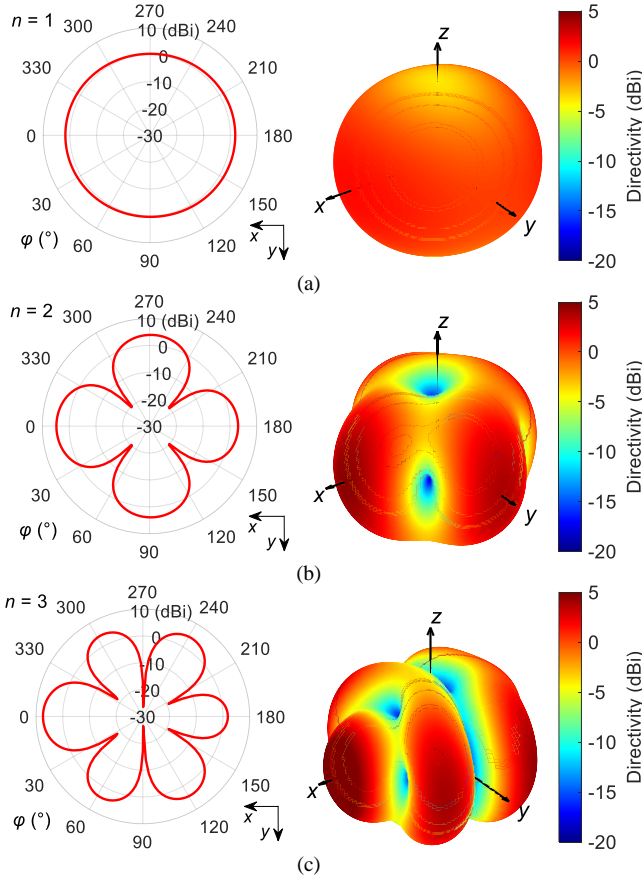


Fig. 10. Directivity patterns of Scenario 1 computed with the SWE method for specific spherical modes: (a)  $n = 1$ , (b)  $n = 2$ , (c)  $n = 3$ . Specifically, these far-field patterns reveal the interaction results between specific excitation modes of the implanted source and the lossy body phantom.

### B. Analysis of a large-scale spherical body model

For a large-scale body model, Fig. 11 shows the model of Scenario 2 and its overall directivity pattern. Like most implanted antennas within large-scale host bodies, the

maximum directivity appears in the positive  $x$ -direction, that is, from the implanted source to the closest interface. Compared to the cases with small-scale host bodies, this result can be explained by the dominance of propagation losses in the lossy host body.

Furthermore, decomposing the overall radiated fields (i.e. EM fields outside the body) into different sets of spherical modes provides insights into the significant propagation losses caused by the large host body. Fig. 12 demonstrates the directivity patterns of Scenario 2 for sets with  $n = 1, 2$ , and 3, respectively. In Table III, an overview of the normalized radiated power and the phase difference in the positive and negative  $x$ -directions for different spherical modes is provided.

According to the normalized radiated power, not only the fundamental spherical modes with  $n = 1$  but also higher-order spherical modes up to  $n = 4$  present a significant contribution to the overall radiated power. This is because of the larger spherical body phantom and the greater offset of the implant within it.

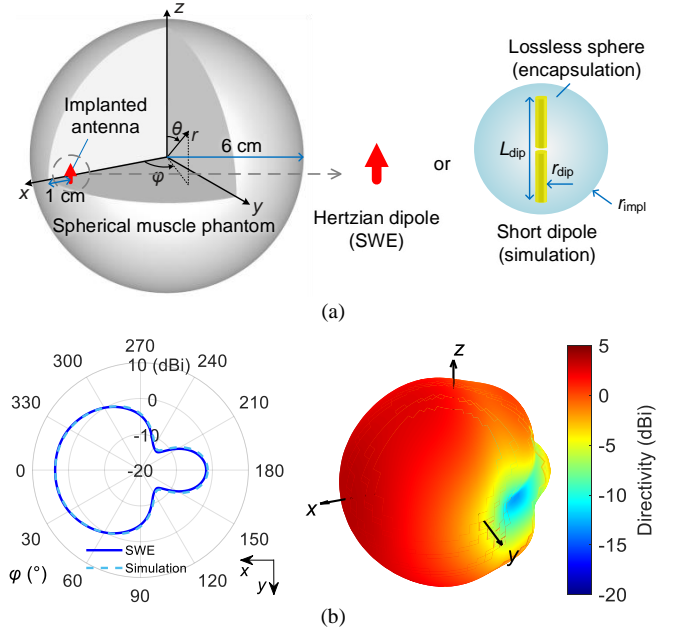


Fig. 11. (a) View of Scenario 2, a large-scale spherical body model. (b) Overall directivity patterns of Scenario 2 computed with the SWE method, where the simulated 2-D pattern is also displayed.

TABLE III  
RADIATED POWER AND PHASE DIFFERENCES OF SPHERICAL MODES IN SCENARIO 2

Mode index $n$	1	2	3	4	5
Normalized radiated power	18.53%	31.22%	36.65%	11.87%	1.58%
Phase difference in positive $x$ -direction	$0^\circ$	$40.66^\circ$	$113.05^\circ$	$-151.15^\circ$	$-69.49^\circ$
Phase difference in negative $x$ -direction	$0^\circ$	$-124.70^\circ$	$148.79^\circ$	$92.89^\circ$	$26.70^\circ$

For the decomposed directivity patterns of different sets of spherical modes (Fig. 12), it can be observed that the radiation patterns are asymmetric with respect to the plane  $x = 0$ , and the main lobes always appear in the positive  $x$ -direction, i.e.,



towards the shortest path to the body–air interface. In contrast, in the negative  $x$ -direction, the directivity is significantly attenuated due to the propagation losses of the body, some even attenuated by more than 10 dB (e.g., the spherical modes with  $n = 1$  or 2). As a result, after superimposing these spherical modes, the overall directivity pattern shown in Fig. 11(b) exhibits the characteristics of typical implanted antennas, i.e., the maximum directivity occurs in the direction of the shortest path from the implant to the body–air interface.

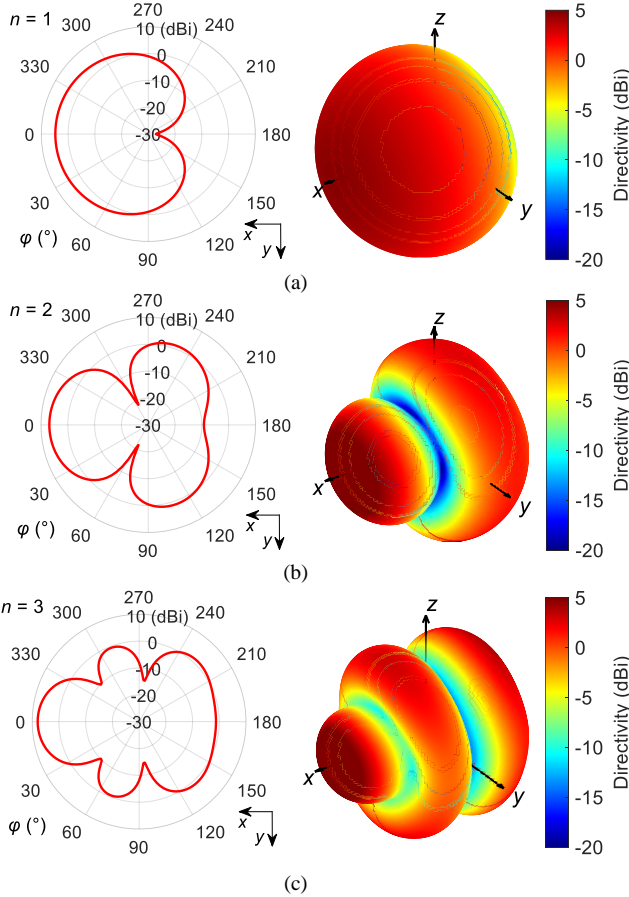


Fig. 12. Directivity patterns of Scenario 2 computed with the SWE method for specific spherical modes: (a)  $n = 1$ , (b)  $n = 2$ , (c)  $n = 3$ . Specifically, these far-field patterns reveal the interaction results between specific excitation modes of the implanted source and the lossy body phantom.

### C. Electromagnetic Resonance of Small-Scale Host Bodies

To further demonstrate the effects of the small-scale host body, Fig. 13 shows the simulated E-field distributions on the cross-sections of the two spherical models. EM waves propagating within the body have a wavelength of 1.69 cm, which can help identify the propagation and scattering processes in these instantaneous E-field distributions. For the small-scale body model [Fig. 13(a)], the entire host body is excited by the implanted antenna, which presents a high-intensity E-field distribution that propagates throughout the body.

Due to the strong reflection at the body–air interface, the host body acts as an EM resonator. Based on this mechanism, the EM waves reaching the free space can be regarded as radiating outward by the entire body–air interface as the antenna

aperture. In contrast, for the large-scale body model [Fig. 13(b)], EM radiation into free space is mostly produced in the vicinity of the body–air interface close to the implanted antenna, while waves propagating through several wavelengths in the body are almost completely attenuated. Based on this mechanism, the maximum directivity occurs in the direction from the implant to the closest body–air interface.

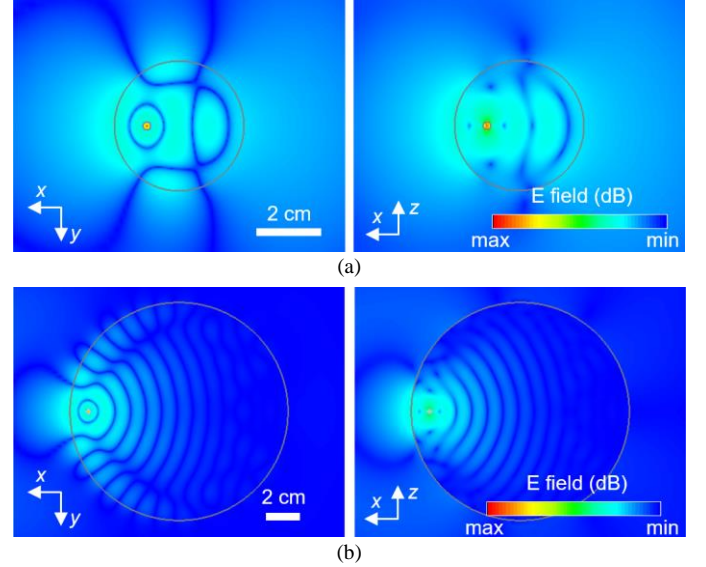


Fig. 13. Simulated instantaneous E-field distributions on the  $x$ - $y$  and  $x$ - $z$  cross-sections of the two spherical models. (a) In Scenario 1, i.e., small-scale host body model, the EM resonance effect within the host body is dominant due to limited body losses. (b) In Scenario 2, i.e., large-scale host body model, the EM waves propagating into the host body are absorbed and thus dampen the resonance effect.

The deformation of directivity pattern caused by small-scale bodies can also be understood from the perspective of dielectric resonator antennas (DRAs), where the excitation of higher-order modes is effectively utilized in antenna gain enhancement, i.e. in deformation of the radiation pattern [47]–[51]. Commonly used DRAs are artificially designed and fabricated using low-lossy dielectrics with high permittivity, e.g., ceramics materials. However, for implanted antennas, the small-scale host body as an EM resonator creates new challenges: The host body is no longer human-designed with predictable low-loss material and shape properties, with even the location of the implant (corresponding to the feed of a DRA) determined in advance according to the specific application. Although small-scale bodies no longer cause significant propagation losses compared to large-scale bodies, near-field losses can still become a significant contributor, especially for implantable wireless devices with thinner encapsulation [35], [37]. Constrained by the limited design scope of the antenna implanted in the small host body, measurement or practical test becomes crucial to determine the judicious placement of external antennas for efficient wireless links.

In addition, various biological tissues in the small animal body induce complex in-body resonance, especially for the excited higher-order modes, resulting in changes and irregularities in the radiation patterns. This means that modeling simplifications of the host bodies of the order of



one-tenth of the wavelength or more could lead to invalid results in numerical simulations of radiation performance.

#### V. A PRACTICAL EXAMPLE: AN OPTOGENETIC IMPLANT WIRELESSLY POWERED BY RF RADIATION

In this section, a prototype of an optogenetic implant powered by RF wireless power transfer is developed to illustrate the importance of analyzing directivity deformation in a practical example.

Fully implantable and wirelessly powered optogenetic implants are commonly used for neuromodulation in the rodent brain or spinal cord [15]. Based on the implantable dipole antenna described in Section II. A., we terminate a similar dipole antenna with an RF rectifier circuit and load a light-emitting diode (LED) on its direct current (DC) terminal, constituting the functional circuit of a wireless optogenetic implant. The details of the rectifier circuit design and device models are the same as described in [6]. With the same matching network design approach, we can match the dipole antenna and the electronic circuit whether in free space or implanted conditions, as shown in Fig. 14(a). For the *ex vivo* demonstration of the prototype, we made a cuboid chicken phantom to test the wireless performance of the optogenetic implant in a small-scale host body. To mimic the body of a small animal, the cuboid chicken model is made of a plastic box (wall thickness of 0.3 mm) filled with chicken muscle tissue and covered with a layer of chicken skin above the implant location. Its detailed dimensions are shown in Fig. 14(b), with a total weight of 12.6 g.

As shown in Fig. 14(c), in the experimental setup, the implant prototype is wirelessly powered by an external RF radiation source operating at 2.40 GHz. The external RF transmitter is comprised of an RF signal generator (SMR20, Rohde & Schwarz) connected to a power amplifier (20 W Outdoor WiFi Signal Booster, Sunhans) as the RF power supply. For directional RF radiation to the target implant, the RF power supply is fed to a transmitting antenna, which is a double-ridged waveguide horn antenna (3115, EMCO).

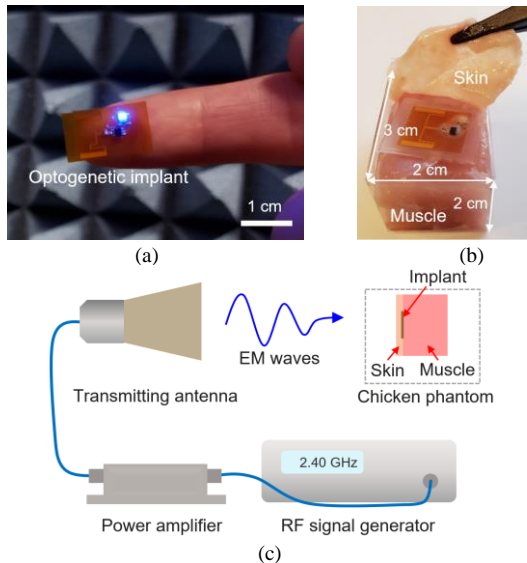


Fig. 14. (a) Photograph of a wireless optogenetic implant on top of the fingertip. (b) Photograph of a cuboid chicken phantom, in which the subcutaneous implant is encapsulated in Ecoflex films with a total thickness of 1 mm. (c) Schematic of the experimental setup for an optogenetic implant powered by RF wireless power transfer.

After implantation in the small-scale chicken phantom, the deformation of the implanted antenna's directivity pattern becomes the dominant factor altering the link efficiency from the transmitting antenna to the implant. Based on the measured results of implanted antennas in rodents, the efficiency of wireless links may vary by more than 10 dB depending on the directions of RF radiation, which ultimately changes the received power.

To understand the angular variations of power receiving capability, we first quantitatively characterized the radiation efficiency and gain of an antenna implanted in cubic chicken phantoms. In a full-wave simulation *via* CST Microwave Studio Suite, we use bio tissues (CST Material Library) to model a cubic chicken phantom and simulate the radiation pattern of a subcutaneously implanted antenna. As shown in Fig. 15, a dipole antenna [same design as the antenna in Fig. 2(a)] is implanted subcutaneously on the front side of the phantom and oriented in the  $y$ -direction. The simulated radiation efficiency of the antenna is  $-15.23$  dB, and the maximum gain of  $-11.16$  dBi appears on the back side of the phantom, specifically in the direction of  $\varphi = 180^\circ$  and  $\theta = 30^\circ$ . Furthermore, we measure the gain pattern of a similar realistic implanted antenna on the  $x$ - $y$  plane using the experimental setup shown in Fig. 2(c), i.e., an independent dipole antenna [Fig. 2(a)] subcutaneously implanted in a cuboid chicken phantom [Fig. 14(b)]. In Fig. 15(b), the measured gain pattern is in good agreement with the simulation results, and the gain in the positive  $x$ -direction is around 3 dB lower than the gain in the negative  $x$ -direction in both results.

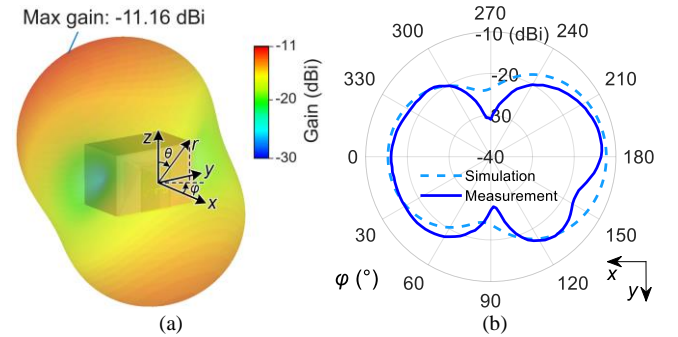


Fig. 15. Gain patterns of the antenna subcutaneously implanted in a cuboid chicken phantom at 2.40 GHz. (a) Simulated 3-D gain pattern, where the main lobe appears on the back side of the phantom. (b) Comparison of simulated and measured gain patterns on the  $x$ - $y$  plane.

In tests of the wireless optogenetic implant, we compare two cases where the RF radiation from the transmitting antenna is directed towards the front side (i.e., the implant is placed under the skin of this side) and the back side of the phantom, as shown in Fig. 15(a) and (b). Taking the maximum distance at which the LED would start to illuminate as an intuitive indicator, we have observed that the maximum distance of the front-side radiation case is 12 cm, while that of the back-side radiation

case reaches 22 cm. In other words, when moved further than these distances, insufficient power was received to illuminate the LED. These test results demonstrate that judicious external antenna placement can effectively improve the efficiency of RF wireless links.

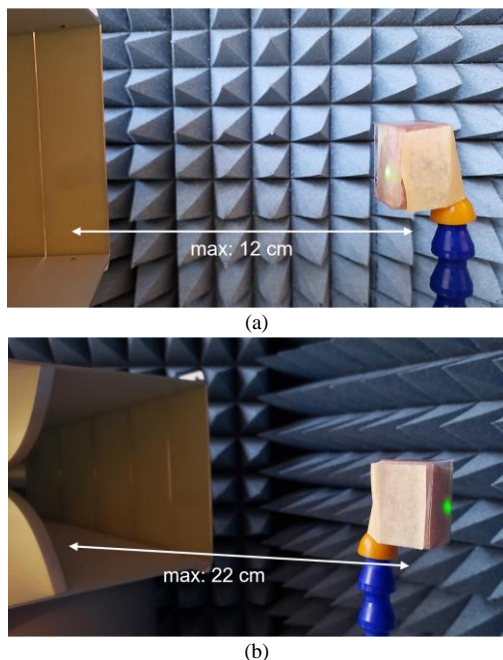


Fig. 16. Photographs of RF wireless power transfer to the optogenetic implant in a cuboid chicken phantom. RF radiation is directed towards (a) the front side of the phantom and (b) the back side.

## VI. CONCLUSION

In this work, we have investigated the key radiation characteristics of implantable RF wireless devices within small animals – the small-scale host body has a great impact on the link efficiency in wireless systems as it deforms its directivity pattern. By analyzing the distribution of EM fields within the body, it is found that the limited propagation losses and the irregular shape of the high-permittivity host body jointly deform the directivity pattern.

From a macroscopic point of view, the body of a small animal works as an EM resonator, and the whole body–air interface can be considered as an antenna aperture that radiates EM waves into the free space. It turns out that the directivity pattern for implants in small-scale host bodies is susceptible to deformations, i.e. it is a function of the host body shape and constitutive parameters as well as the implant location and orientation. As a next step, the effect of body motion and deformation on the radiation pattern could be further investigated.

In practice, as demonstrated in the example of an RF wireless-powered optogenetic implant, knowledge of the directivity pattern deformation contributes to a several-fold increase in the link efficiency through the optimal placement of the external link antenna. Using a cuboid chicken phantom, it was observed numerically and experimentally, that the radiation gain towards the closest air-body interface can be up to 3 dB lower than the radiation towards the opposite direction. The findings presented in this paper underscore the challenges

and importance of carefully designing implantable RF wireless devices for small-scale animals, as the relative electrical dimensions of the body and implant placement will critically affect the wireless link budget.

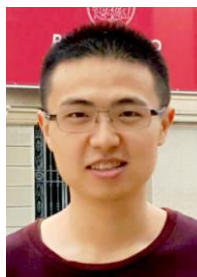
## ACKNOWLEDGMENT

The authors acknowledge with gratitude the assistance from Dr. Alexandre Widmer for the preparation of the animal cadavers used in the experiment, and from Ivan Furfaro for his help in building the measurement platform.

## REFERENCES

- [1] D. Fitzpatrick, *Implantable Electronic Medical Devices*. New York, NY, USA: Elsevier, 2014.
- [2] A. Kiourt, K. A. Psathas, and K. S. Nikita, “Implantable and ingestible medical devices with wireless telemetry functionalities: A review of current status and challenges,” *Bioelectromagnetics*, vol. 35, no. 1, pp. 1–15, 2014.
- [3] A. Bansal, F. Yang, T. Xi, Y. Zhang, and J. S. Ho, “In vivo wireless photonic photodynamic therapy,” *Proc. Nat. Acad. Sci. USA*, vol. 115, no. 7, pp. 1469–1474, Feb. 2018.
- [4] S. Carrara, “Body dust: well beyond wearable and implantable sensors,” *IEEE Sensors J.*, vol. 21, no. 11, pp. 12398–12406, Jun. 2021.
- [5] J. S. Ho *et al.*, “Self-Tracking Energy Transfer for Neural Stimulation in Untethered Mice,” *Phys. Rev. Appl.*, vol. 4, no. 2, Aug. 2015.
- [6] K. L. Montgomery, *et al.*, “Wirelessly powered, fully internal optogenetics for brain, spinal and peripheral circuits in mice,” *Nature Methods*, vol. 12, no. 10, pp. 969–974, Oct. 2015.
- [7] S. I. Park, *et al.*, “Soft, stretchable, fully implantable miniaturized optoelectronic systems for wireless optogenetics,” *Nat. Biotechnol.*, vol. 33, no. 12, pp. 1280–1286, Nov. 2015.
- [8] S. I. Park, *et al.*, “Stretchable multichannel antennas in soft wireless optoelectronic implants for optogenetics,” *Proc. Nat. Acad. Sci. USA*, vol. 113, no. 50, pp. E8169–E8177, 2016.
- [9] K. N. Noh, *et al.*, “Miniaturized, battery-free optofluidic systems with potential for wireless pharmacology and optogenetics,” *Small*, vol. 14, no. 4, 2018.
- [10] A. D. Mickle, *et al.*, “A wireless closed-loop system for optogenetic peripheral neuromodulation,” *Nature*, 565 (7739), pp. 361–365, 2019.
- [11] S. Idogawa, *et al.*, “A lightweight, wireless Bluetooth-low-energy neuronal recording system for mice,” *Sensors and Actuators B: Chemical*, Volume 331, 2021.
- [12] C. Y. Kim, *et al.*, “Soft subdermal implant capable of wireless battery charging and programmable controls for applications in optogenetics,” *Nat. Commun.*, vol. 12, no. 1, Jan. 2021.
- [13] C. Kathe, *et al.*, “Wireless closed-loop optogenetics across the entire dorsoventral spinal cord in mice,” *Nat. Biotechnol.*, vol. 40, no. 2, p. 198–208, 2021.
- [14] J. P. Wright, *et al.*, “A fully implantable wireless bidirectional neuromodulation system for mice,” *Biosens. Bioelectron.*, 200, 113886, 2022.
- [15] S. M. Won, L. Cai, P. Gutruf, and J. A. Rogers, “Wireless and battery-free technologies for neuroengineering,” *Nat. Biomed. Eng.*, vol. 7, no. 4, 405–423, 2023.
- [16] A. Yakovlev, S. Kim, and A. S. Y. Poon, “Implantable biomedical devices: Wireless powering and communication,” *IEEE Commun. Mag.*, vol. 50, no. 4, pp. 152–159, Apr. 2012.
- [17] C. Liu, Y.-X. Guo, and S. Xiao, “A review of implantable antennas for wireless biomedical devices,” in *Proc. Forum Electromagn. Res. Methods Appl. Technol. (FERMAT)*, 2016, pp. 1–11.
- [18] A. Kiourt and K. S. Nikita, “A review of in-body biotelemetry devices: Implantables, ingestibles, and injectables,” *IEEE Trans. Biomed. Eng.*, vol. 64, no. 7, pp. 1422–1430, 2017.
- [19] A. K. Teshome, B. Kibret, and D. T. H. Lai, “A review of implant communication technology in WBAN: progress and challenges,” *IEEE Rev. Biomed. Eng.*, vol. 12, pp. 88–99, 2019.

- [20] Z. Xie, R. Avila, Y. Huang, and J. A. Rogers, "Flexible and Stretchable Antennas for Biointegrated Electronics," *Advanced Materials*, vol. 32, no. 15, p. 1902767, Sep. 2019.
- [21] G. Schiavone, *et al.*, "Soft, implantable bioelectronics for translational research," *Adv. Mater.*, vol. 32, no. 17, p.1906512, 2020.
- [22] J. Zhu, *et al.*, "Strain-Insensitive Hierarchically Structured Stretchable Microstrip Antennas for Robust Wireless Communication," *Nano-Micro Letters*, vol. 13, no. 1, Apr. 2021.
- [23] S. Zhang, *et al.*, "Standalone stretchable RF systems based on asymmetric 3D microstrip antennas with on-body wireless communication and energy harvesting," *Nano Energy*, vol. 96, p. 107069, Jun. 2022.
- [24] A. Kiourti, *et al.*, "Next-generation healthcare: Enabling technologies for emerging bioelectromagnetics applications," *IEEE Open J. Antennas Propag.*, vol. 3, pp. 363–390, 2022.
- [25] F. Merli, "Implantable antennas for biomedical applications," Ph.D. dissertation, Dept. Elect. Eng., Swiss Federal Inst. Technol. Lausanne (EPFL), Lausanne, Switzerland, 2011.
- [26] E. Y. Chow, M. M. Morris and P. P. Irazoqui, "Implantable RF Medical Devices: The Benefits of High-Speed Communication and Much Greater Communication Distances in Biomedical Applications," *IEEE Microw. Mag.*, vol. 14, no. 4, pp. 64–73, June 2013.
- [27] C. T. Tai and R. E. Collin, "Radiation of a Hertzian dipole immersed in a dissipative medium," *IEEE Trans. Antennas Propag.*, vol. 48, no. 10, pp. 1501–1506, Oct. 2000.
- [28] A. Karlsson, "Physical limitations of antennas in a lossy medium," *IEEE Trans. Antennas Propag.*, vol. 52, no. 8, pp. 2027–2033, Aug. 2004.
- [29] J. Kim and Y. Rahmat-Samii, "Implanted antennas inside a human body: simulations, designs, and characterizations," *IEEE Trans. Microw. Theory Tech.*, vol. 52, no. 8, pp. 1934–1943, Aug. 2004.
- [30] A. S. Y. Poon, S. O. Driscoll, and T. H. Meng, "Optimal frequency for wireless power transmission into dispersive tissue," *IEEE Trans. Antennas Propag.*, vol. 58, no. 5, pp. 1739–1750, 2010.
- [31] F. Merli, B. Fuchs, J. R. Mosig, and A. K. Skrivervik, "The effect of insulating layers on the performance of implanted antennas," *IEEE Trans. Antennas Propag.*, vol. AP-59, no. 1, pp. 21–31, Jan. 2011.
- [32] S. Kim, J. S. Ho, L. Y. Chen, and A. S. Y. Poon, "Wireless power transfer to a cardiac implant," *Appl. Phys. Lett.*, vol. 101, pp. 073701, Aug. 2012.
- [33] D. P. Chrissoulidis and J.-M. Laheurte, "Radiation from an encapsulated Hertz dipole implanted in a human torso model," *IEEE Trans. Antennas Propag.*, vol. 64, no. 12, pp. 4984–4992, Dec. 2016.
- [34] D. Nikolayev, W. Joseph, M. Zhadobov, R. Sauleau, and L. Martens, "Optimal radiation of body-implanted capsules," *Phys. Rev. Lett.*, vol. 122, no. 10, p. 108101, Mar. 2019.
- [35] A. Skrivervik, M. Bosiljevac, and Z. Šipuš, "Fundamental limits for implanted antennas: maximum power density reaching free space," *IEEE Trans. Antennas Propag.*, vol. 67, no. 8, pp. 4978–4988, Aug. 2019.
- [36] M. Gao, Z. Šipuš, and A. K. Skrivervik, "On the maximum power density of implanted antennas within simplified body phantoms," in *Proc. 16th Eur. Conf. Antennas Propag. (EuCAP 2022)*, Madrid, Spain, 2022, pp. 1–5.
- [37] M. Gao, Z. Šipuš, and A. K. Skrivervik, "Analytic Approximation of In-Body Path Loss for Implanted Antennas," *IEEE Open J. Antennas Propag.*, 2023.
- [38] S. Hout and J. Chung, "Design and Characterization of a Miniaturized Implantable Antenna in a Seven-Layer Brain Phantom," *IEEE Access*, vol. 7, pp. 162062–162069, 2019.
- [39] S. Gabriel, R.W. Lau, and C. Gabriel, "The dielectric properties of biological tissues: III. Parametric models for the dielectric spectrum of tissues," *Phys. Med. Biol.*, vol. 41, 2271, 1996.
- [40] J. A. Stratton, *Electromagnetic Theory*. New York, NY, USA: McGraw-Hill, 1941.
- [41] R. F. Harrington, *Time-Harmonic Electromagnetic Fields*. New York, NY, USA: McGraw-Hill, 1961.
- [42] S. Stein, "Addition theorems for spherical wave functions," *Quart. Appl. Math.*, vol. 19, pp. 15–24, 1961.
- [43] W. C. Chew, *Waves and Fields in Inhomogeneous Media*. Piscataway, NJ, USA: IEEE Press, 1995.
- [44] F. Jensen and A. Frandsen, "On the number of modes in spherical wave expansion," in *Proc. AMTA-2004*, Oct. 2004, pp. 489–494.
- [45] M. Bosiljevac, Z. Šipuš, and A. K. Skrivervik, "Propagation in finite lossy media: An application to WBAN," *IEEE Antenn. Wireless Propag. Lett.*, vol. 14, pp. 1546–1549, 2015.
- [46] D. Tayli, M. Capek, L. Akrou, V. Losenicky, L. Jelinek and M. Gustafsson, "Accurate and Efficient Evaluation of Characteristic Modes," *IEEE Trans. Antennas Propag.*, vol. 66, no. 12, pp. 7066–7075, Dec. 2018.
- [47] A. Petosa, *Dielectric Resonator Antenna Handbook*. Norwood, MA: Artech House, 2007.
- [48] A. Petosa and A. Ittipiboon, "Dielectric Resonator Antennas: A Historical Review and the Current State of the Art," *IEEE Antennas Propag. Mag.*, vol. 52, no. 5, pp. 91–116, Oct. 2010.
- [49] Y. -M. Pan, K. W. Leung, and K. -M. Luk, "Design of the Millimeter-wave Rectangular Dielectric Resonator Antenna Using a Higher-Order Mode," *IEEE Trans. Antennas Propag.*, vol. 59, no. 8, pp. 2780–2788, Aug. 2011.
- [50] K. W. Leung, E. H. Lim, and X. S. Fang, "Dielectric Resonator Antennas: From the Basic to the Aesthetic," *Proceedings of the IEEE*, vol. 100, no. 7, pp. 2181–2193, July 2012.
- [51] M. Mmka and Z. Raida, "Enhanced-gain dielectric resonator antenna based on the combination of higher-order modes," *IEEE Antennas Wireless Propag. Lett.*, vol. 15, pp. 710–713, 2016.



**Mingxiang Gao** received the double B.Sc. degree in electrical engineering and business administration and the first M.Sc. degree in electrical engineering from Xi'an Jiaotong University, Xi'an, China, in 2016 and 2019, respectively, and the second M.Sc. degree (summa cum laude) in electrical engineering from the Politecnico di Milano, Milan, Italy, in 2019. He is currently pursuing the Ph.D. degree in electrical engineering with the Ecole Polytechnique Fédérale de Lausanne, Lausanne, Switzerland. His research interests include the theory and design of implantable antennas, wireless techniques for bioelectronics, numerical techniques for electromagnetics, and bioelectromagnetics.



**James D. Rosenthal (Member, IEEE)** received the B.S. degree in electrical engineering from the University of Minnesota, Minneapolis, MN, USA, in 2013, and the M.S. and Ph.D. degrees in electrical engineering from the University of Washington, Seattle, WA, USA, in 2018 and 2021, respectively. From 2013 to 2016, he was an Electrical Engineer with the NASA Langley Research Center, Hampton, VA, USA, where he designed avionics systems for aerospace research. From 2016 to 2021, he was a Research Assistant and an NSF Graduate Research Fellow with the Department of Electrical and Computer Engineering, University of Washington. He is currently a Marie Skłodowska-Curie Postdoctoral Research Fellow with the Swiss Federal Institute of Technology Lausanne (EPFL), Lausanne, Switzerland. His research focuses on the design of ultralow-power backscatter communication systems for bioelectronic medical devices.





**Kangling Wu** received the B.Sc. degree in mechanical engineering and the M.Sc. degree in mechanical engineering from Xi'an Jiaotong University, Xi'an, China, in 2016 and 2019, respectively. She is currently pursuing the Ph.D. degree in mechanical engineering at the Ecole Polytechnique Fédérale de Lausanne (EPFL), Lausanne, Switzerland. Her research focuses on the microfabrication of flexible/stretchable neural interfaces and design of thin-film encapsulation for chronic neural implants.



**Zvonimir Sipus (Senior Member, IEEE)** received the B.Sc. and M.Sc. degrees in electrical engineering from the University of Zagreb, Zagreb, in 1988 and 1991, respectively, and the Ph.D. degree in electrical engineering from the Chalmers University of Technology, Gothenburg, Sweden, in 1997. From 1988 to 1994, he was with Rudjer Boskovic Institute, Zagreb, as a Research Assistant, where he was involved in the development of detectors for explosive gasses. In 1994, he joined the Antenna Group, Chalmers University of Technology, where he was involved in research projects concerning conformal antennas and soft and hard surfaces. In 1997, he joined the Faculty of Electrical Engineering and Computing, University of Zagreb, where he is currently a Professor. From 1999 to 2005, he was also an Adjunct Researcher with the Department of Electromagnetics, Chalmers University of Technology. Since 2006, he has been involved in teaching with the European School of Antennas. From 2008 to 2012 and from 2014 to 2018, he was the Head of the Department of Wireless Communications. His current research interests include the analysis and design of electromagnetic structures with application to antennas, microwaves, and optical communication and sensor systems.



**Stéphanie P. Lacour (Member, IEEE)** received the Ph.D. degree in electrical engineering from the INSA de Lyon, Villeurbanne, France, in 2001. She was a Post-Doctoral Research with Princeton University, Princeton, NJ, USA, and the University of Cambridge, Cambridge, U.K. She joined the École Polytechnique Fédérale de Lausanne, Lausanne, Switzerland, in 2011, where she holds the Bertarelli Foundation Chair in neuroprosthetic technology with the School of Engineering and the Director of the interdisciplinary Neuro-X Institute. Dr. Lacour was a recipient of the 2006 MIT TR35, the ERC StG in 2011, and the SNSF ERC CG in 2016. She was nominated as a 2015 Young Global Leader by the World Economic Forum.



**Anja K. Skriver** received the master's degree in electrical engineering and the Ph.D. degree from the Ecole Polytechnique Fédérale de Lausanne (EPFL), Lausanne, Switzerland, in 1986 and 1992, respectively. She was an Invited Research Fellow with the University of Rennes, Rennes, France, followed by two years in the industry. In 1996, she rejoined EPFL as an Assistant Professor, where she is currently a Full Professor and also the Head of the Microwaves and Antennas Group. She was the Director of the EE Section from 1996 to 2000, and is currently the Director of the EE Doctoral School with EPFL. Her teaching activities include courses on microwaves and antennas and courses at Bachelor, Master, and Ph.D. levels. She has authored or coauthored more than 200 peer-reviewed scientific publications. Her current research interests include electrically small antennas, antennas in biological media, multifrequency and ultrawideband antennas, and numerical techniques for electromagnetics. She was the recipient of the Latsis Award. She is frequently requested to review research programs and centres in Europe. She was the Chairperson of the Swiss URSI until 2012. She is very active in European collaboration and European Projects. Since 2017, she has been a member of the Board of Directors of the European Association on Antennas and Propagation and is a Board Member of the European School on Antennas.